

FAKULTÄT FÜR PHYSIK PHYSIKALISCHES PRAKTIKUM FÜR FORTGESCHRITTENE PRAKTIKUM MODERNE PHYSIK

Gruppe Nr.:	20				
Kurs:	□ Mo1 ⊠ Mo2 □ Mi3				
aktuelles Semester:	SoSe 2025				
Versuch:	Properties of cosmic muons				
Namen:	Andreas Pfeffer				
	Johannes Engel				
Assistent:	Tatiana Selezneva				
durchgeführt am:	05.05.2025				
Protokollabgabe am:	23.05.2025				
vom Betreuer auszufüllen					
Note gesamt + 0 -					
Anerkannt:					
(Datum Unterschrift)					
Datum Rückgabe:					
Bemerkung:					

Contents

1	Intr	oduction	3			
	1.1	Extensive air showers (EASs)	3			
	1.2	Muons in matter	5			
	1.3	Parity violation	6			
	1.4	Positron angular spectrum	6			
	1.5	Magnetic Moment and Spin Precession	7			
	1.6	Muon Lifetime and Spin-Precession Measurements	7			
2	Det	ermination of the noise threshold of the detectors	9			
	2.1	Method	9			
	2.2	Analysis	9			
	2.3	Results	9			
	2.4	Conclusion	10			
3	Rec	ording a pulse height spectrum	10			
	3.1	(a) Using internal triggers	10			
	3.2	(b) Use of external triggers	11			
4	Determination of the efficiency of the individual detector modules					
5	Det	ermination of the lifetime of the muon	14			
	5.1	Evaluation of Muon Lifetime Data	14			
		5.1.1 Data Processing	14			
		5.1.2 Exponential Decay Fit	14			
		5.1.3 Background Correction	15			
	5.2	Resulting Muon Lifetime	15			
6	Pro	of of the precession of the muon spin in the magnetic field and determination of				
	the	statistical significance	17			
	6.1	Physical Principle	17			
	6.2	Data Processing	17			
	6.3	Fit Procedure	17			
	6.4	Comparison of Exponential and Spin-Modulated Fits	18			
		6.4.1 Fit Results and Significance Test	19			
	6.5	Extraction of Physical Quantities	19			
		6.5.1 Magnetic Field Estimation	19			
		6.5.2 Theoretical Larmor Frequency	20			
		6.5.3 Measured Precession Frequencies and Comparison	20			
		6.5.4 Discussion	20			

1 Introduction

Generally, cosmic rays are highly energetic particles travelling through the Universe. These particles provide insights into astrophysical phenomena and the interstellar medium, including the magnetic fields they traverse, their possible origins, how they were accelerated and their mass composition. In the history of particle and high-energy particle physics, cosmic rays played a fundamental role since their discovery in 1912 by Victor Hess [Hess]. Until now, there have been multiple experiments that have detected astroparticles and their properties. Different experiments analyzed different parts of the spectrum of these arriving particles. The spectrum of cosmic rays can be described by a power law

$$\frac{N}{E} \propto E^{-\gamma},\tag{1}$$

in the wide range of energies from $10^9\,\text{eV}$ to $10^{20}\,\text{eV}$ as shown in Fig. 1 where the spectral index γ is changing with energy and has several "breaks". Below the so called knee (energies of 4×10^{15} eV and less) γ is estimated to be 2.7. The spectrum steepens, resulting in a higher spectral index of 3.1 up to the second knee at 4×10^{17} eV. Between the second knee and the ankle at 4×10^{18} eV γ is at 3.3. Particles beyond the ankle are called UHECRs (Ultra-High-Energy Cosmic Rays). The cosmic-ray spectrum below 10¹⁸ eV is believed to originate from galactic sources [flux]. The knee may indicate that most galactic accelerators, such as expanding supernova remnants, have reached their energy limits. These remnants are estimated to accelerate protons only up to around 10^{15} eV. Additionally, the propagation of cosmic rays within the galaxy could contribute to this spectral feature. The second knee is believed to originate from a transition to heavier primary particles in this range. The ankle is believed to represent the dominance of an extragalactic cosmic-ray population over the galactic one. Alternatively, it could arise from the energy losses of extragalactic protons interacting with the cosmic microwave background (CMB) through pair production. This interpretation supports the idea that the highest-energy cosmic rays are primarily extragalactic protons, with minimal galactic contribution above 10^{18} eV. This is consistent with the energy limits of supernova remnants [flux]. As shown in Fig. 1, the higher the energies of the primaries, the lesser particles are observed. To measure the spectrum with energies below the knee, it is possible to place small detectors in space for direct detection. This method is not suitable for energies above the knee because particles with such high energies are very rare. At the knee, the flux is roughly 1 particle per square meter and 100 days. So, placing a detector in space to perform direct measurements is just sufficient to detect particles with up to 10^{14} eV because it is too expensive to place a large detector in space or to wait many years for statistically significant results.

1.1 Extensive air showers (EASs)

EASs are cascades of secondary particles traversing through Earth's atmosphere. When a primary cosmic ray enters the atmosphere, it interacts with a nucleus in the air, secondary particles are produced, and these secondary particles decay into other particles or interact with additional nuclei in the air. This process occurs multiple times, causing a shower to develop. The shower size increases while traveling through Earth's atmosphere. This cascade spreads while moving through the air almost with the speed of light towards the surface of Earth. It is highly unlikely that the primary particle reaches the ground due to energy loss and interaction processes, and therefore its properties have to be reconstructed by analyzing the cascade it produced [Heitler]. This phenomenon is described by the Heitler model, which is illustrated in Fig. 2a. The EAS contains a hadronic (right side of Fig. 2a) and an electromagnetic cascade (left side of Fig. 2a). The hadronic component is located near the shower core and contains barions, pions, kaons and neutrinos. The neutral pions decay almost entirely in photons contributing to the electromagnetic cascade. Electrons and positrons produce photons via bremsstrahlung

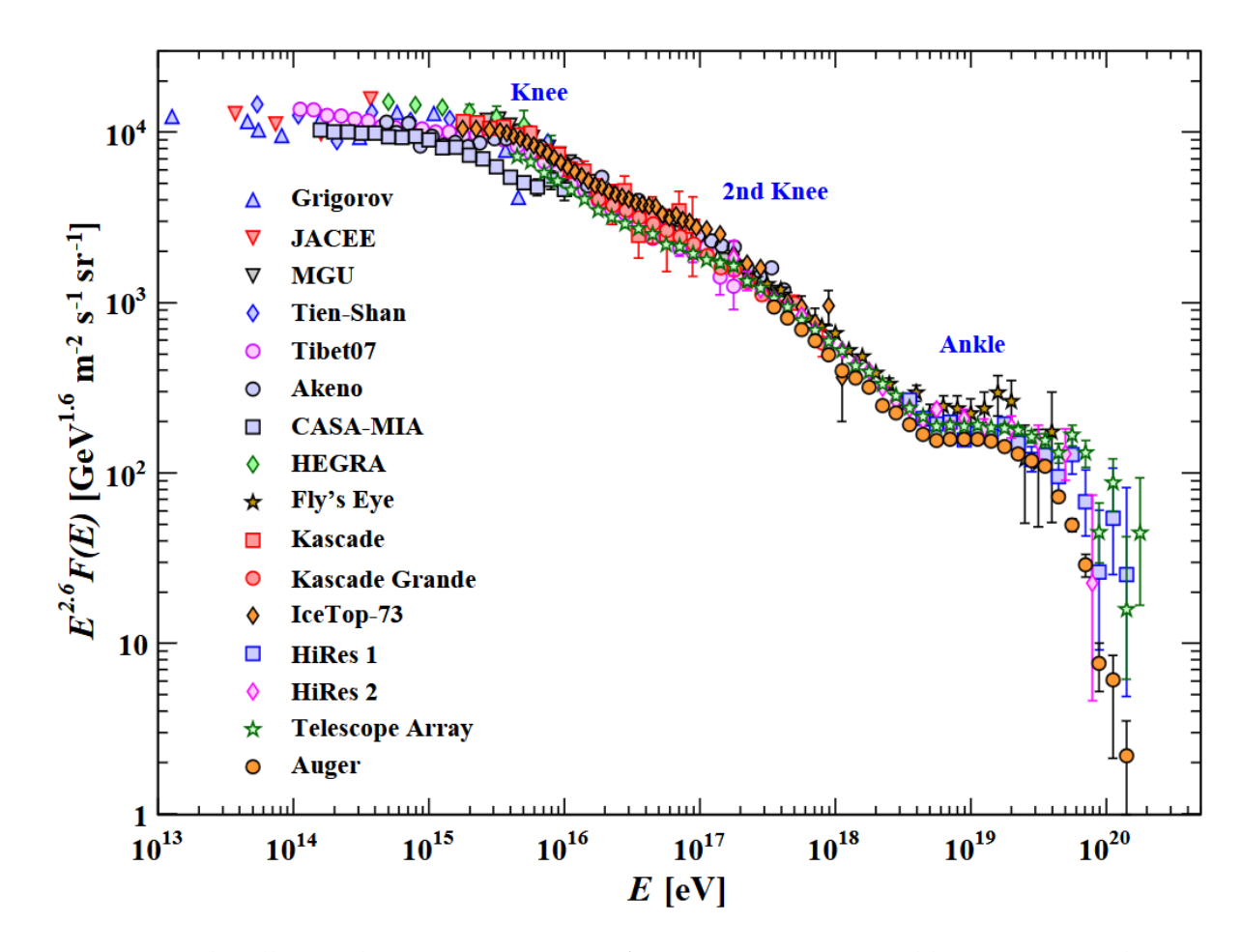


Figure 1: The all-particle energy spectrum of cosmic rays, measured by various air-shower experiments over several decades of energy. The most prominent features of the spectrum are highlighted at their corresponding energies. Source: Ref. [flux].

in the presence of the field of a nuclei N. Photons on the other hand produce electrons and positrons via pair production near nuclei N [Heitler].

$$\pi^0 \to 2\gamma$$
 ($\approx 99\%$, $\tau = 8.4 \times 10^{-17} \,\mathrm{s}$) (2)

$$\pi^0 \to e^+ + e^- + \gamma \quad (\approx 1\%) \tag{3}$$

$$e^{\pm} + N \rightarrow N + e^{\pm} + \gamma \tag{4}$$

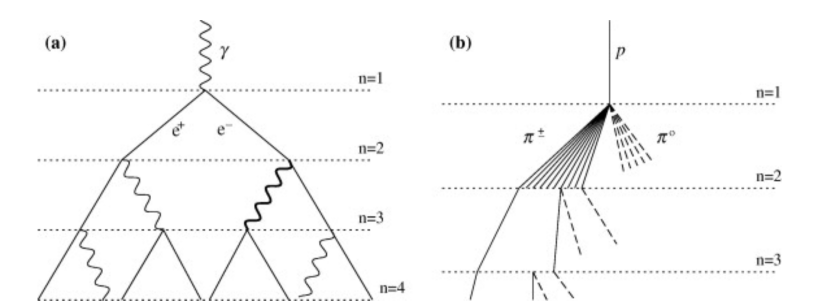
$$\gamma + N \rightarrow N + e^+ + e^- \tag{5}$$

Only kaons and charged pions contribute to the hadronic component of the shower. Even some kaons or charge pions decay into muons [pdg],

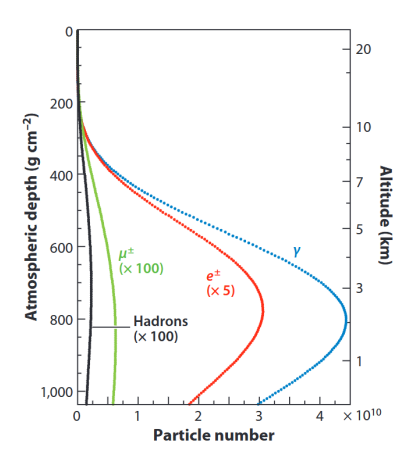
$$\pi^{\pm} \to \mu^{\pm} + \stackrel{(-)}{\nu_{\mu}} \qquad (\tau = 2.6 \times 10^{-8} \,\mathrm{s}),$$
 (6)

$$K^{\pm} \to \mu^{\pm} + \stackrel{(-)}{\nu_{\mu}}$$
 (7)

99% of the particles in the shower are photons, electrons, and positrons, which are part of the electromagnetic shower [altitude]. These particles carry 80 to 90% of the total energy of the EAS. Muons carry about 10% of the energy despite being rare compared to electrons, positrons, and photons. The cascade loses energy while it is forming and therefore its particle number and size of the plane front decreases with time and travel distance. For this reason, it is advantageous to place detectors at higher altitudes, where the cascade is still more developed



(a) Illustrations of (a) an electromagnetic cascade and (b) a hadronic shower described by the Heitler model. In the hadronic shower, the dashed lines represent neutral pions, which do not undergo further interactions but rapidly decay to produce electromagnetic subshowers (not depicted in the diagram). For clarity, not all pion tracks are displayed. Both diagrams are schematic and not drawn to scale. Source: Ref. [Heitler].



(b) Longitudinal shower profiles for vertical, proton-induced showers at 10¹⁹ eV. Source: Ref. [altitude].

Figure 2: Characteristics of Extensive Air Showers (EAS)

and contains a higher density of particles like illustrated in Fig. 2b. Muons, however, are still more abundant in lower altitudes and even penetrate Earth's surface due to their relatively "slow" decay [BlueBook]

$$\mu^{\pm} \to e^{\pm} + \stackrel{(-)}{\nu_{\mu}} + \stackrel{(-)}{\nu_{e}} \qquad (\tau = 2.19 \times 10^{-6} \,\text{s}).$$
 (8)

The relatively long lifetime of the muon is caused by its mass. Muons are ≈ 200 times heavier than an electron, so the probability of generating electromagnetic cascades is much smaller for muons. This interrelation is described by the equation of the intensity of bremsstrahlung [BlueBook],

$$I \propto \frac{z^2 Z^2}{m^2}. (9)$$

The lifetime of the muon is not sufficiently long enough to explain their abundance at sea level when not taking into account time dilation. Eq. (8) is measured in the rest frame of the muon. The lifetime of muons in the rest frame of the Earth is calculated by

$$\tau_E = \gamma \tau_{\mu}. \tag{10}$$

1.2 Muons in matter

High-energy muons slow by bremsstrahlung, with ionization becoming relevant only below GeV energies—processes independent of charge. Near rest, however, μ^- and μ^+ diverge:

- Negative muons (μ^-): Captured into atomic orbits, they cascade to the K-shell emitting X-rays, then undergo nuclear capture. This extra decay channel shortens their lifetime (in Cu, $\tau \approx 1.63 \times 10^{-7}$ s), so almost all μ^- disappear within a microsecond.
- **Positive muons** (μ^+): Bind electrons to form neutral muonium, rapidly ionize and recombine ($\approx 5 \times 10^{-13}$ s), then thermalize ($\approx 10^{-12}$ s), but do not undergo nuclear capture.

Thus, although both charge states lose energy similarly at high speed, μ^- vanish quickly at low energy while μ^+ persist until their natural decay.

1.3 Parity violation

When charged pions at rest decay via the weak interaction, the muon and neutrino helicities are fixed by angular-momentum and parity-violation constraints. A spin 0 π^+ produces a left-handed (negative-helicity) ν_μ , so the μ^+ must also emerge with "wrong" (negative) helicity—even though phase-space would favor the lighter positron. In the pion's lab frame this leads to two energy groups: muons born forward carry almost the full pion energy, those born backward much less. Their spins remain opposite to their momenta in the high-energy branch and parallel in the low-energy branch.

Because the cosmic-ray pion spectrum falls steeply with energy, more low-energy muons arise from forward decays than from backward decays at that same energy. Stopped μ^+ in a copper absorber therefore exhibit a net negative polarization (spin opposite to flight direction), empirically about -1/3 for perpendicular incidence. Averaging over all angles reduces the magnitude only slightly.

Once thermalized, muons (free or in muonium) slow so rapidly that they do not precess appreciably before stopping. Subsequent depolarization driven by local magnetic inhomogeneities in the host material occurs on time scales ($\gg 5\times 10^{-5}\,\mathrm{s}$ in copper at room temperature) far longer than the muon's $\approx 2\times 10^{-6}\,\mathrm{s}$ lifetime. Thus the initial polarization is effectively preserved until decay.

1.4 Positron angular spectrum

When a polarized muon μ^+ decays, the double-differential distribution of emitted positrons in energy and angle is given by

$$\frac{\mathrm{d}N}{\mathrm{d}\varepsilon\,\mathrm{d}\Omega} = \frac{\varepsilon^2}{2\pi} \Big[(3 - 2\varepsilon) - P(1 - 2\varepsilon)\cos\theta \Big] \quad , \quad \varepsilon = \frac{E}{E_{\mathrm{max}}}, \ E_{\mathrm{max}} = \frac{m_{\mu}c^2}{2}, \tag{11}$$

where P is the muon polarization and θ the angle between positron momentum and muon spin. One may rewrite this in the form

$$\frac{\mathrm{d}N}{\mathrm{d}\varepsilon\,\mathrm{d}\Omega} = a(\varepsilon)\left[1 + b(\varepsilon)\,\cos\theta\right],\tag{12}$$

with an energy-dependent asymmetry parameter $b(\varepsilon)$ ranging from -1/3 at $\varepsilon \to 0$ up to +1 at $\varepsilon = 1$. Thus:

- Low-energy positrons ($\varepsilon \ll 1$) are nearly isotropic ($b \approx -1/3$), and many are lost below detector threshold.
- High-energy positrons ($\varepsilon \approx 1$) exhibit strong forward–backward asymmetry ($b \approx 1$), preferentially along the muon spin.

Integrating over energy above a detection threshold yields

$$\frac{\mathrm{d}N}{\mathrm{d}\Omega} = k \left[1 + A \cos \theta \right],\tag{13}$$

where the observed asymmetry A depends on threshold. For the full spectrum A = P/3, while restricting to the upper half of the energy range gives $A \approx 0.44 \, P$. Raising the threshold further increases A toward P but reduces the count rate, requiring a balance between polarization sensitivity and statistics.

1.5 Magnetic Moment and Spin Precession

A particle with angular momentum J carries a magnetic moment

$$\mu = \gamma \mathbf{J}, \tag{14}$$

where γ is the gyromagnetic ratio. In a uniform magnetic field **B** the torque

$$\frac{\mathrm{d}\mathbf{J}}{\mathrm{d}t} = \boldsymbol{\mu} \times \mathbf{B} \tag{15}$$

causes **J** (and thus μ) to precess around **B** with angular frequency

$$\omega = \gamma B. \tag{16}$$

The gyromagnetic ratio can be expressed in terms of the dimensionless g-factor and the Bohr magneton μ_B as

$$\gamma = \frac{g \,\mu_B}{\hbar} \,. \tag{17}$$

For an electron

$$\mu_B(e) = \frac{e \, \hbar}{2 \, m_e} \approx 9.273 \times 10^{-24} \, \text{J/T} \,,$$
 (18)

and for a muon

$$\mu_B(\mu) = \frac{e \, \hbar}{2 \, m_\mu} = \frac{m_e}{m_\mu} \, \mu_B(e) \approx 4.485 \times 10^{-26} \, \text{J/T} \,.$$
 (19)

The *g*-factor (Landé factor) characterizes the proportionality between spin and magnetic moment. For orbital motion g=1, while for a spin- $\frac{1}{2}$ particle quantum corrections shift g slightly above 2. Experimentally one extracts g by measuring the precession frequency ω in a known field B via

$$g = \frac{\gamma \hbar}{\mu_B} = \frac{h \,\omega}{\mu_B \,B} \,. \tag{20}$$

1.6 Muon Lifetime and Spin-Precession Measurements

The muon mean lifetime τ is obtained by stopping muons in the detector, marking t=0 when they come to rest and recording the positron emission time; over many events the count follows

$$N(t) = N_0 e^{-t/\tau}, (21)$$

where N_0 is the number of stopped muons. To measure the spin-precession frequency ω , a uniform magnetic field is applied transverse to the muon beam so that the muon spin precesses, and only positrons emitted in a fixed direction are counted; this yields a time spectrum

$$N(t) = K e^{-t/\tau} \left[1 + \bar{A}\cos(\omega t + \delta) \right], \tag{22}$$

with K a normalization constant, \bar{A} the averaged geometrical asymmetry and δ an initial phase. If the muon polarization relaxes with characteristic time T_R the asymmetry decays as

$$\bar{A}(t) = \bar{A}_0 e^{-t/T_R},$$
 (23)

though in materials such as copper T_R is long enough that \bar{A} can be taken constant over the measurement interval.

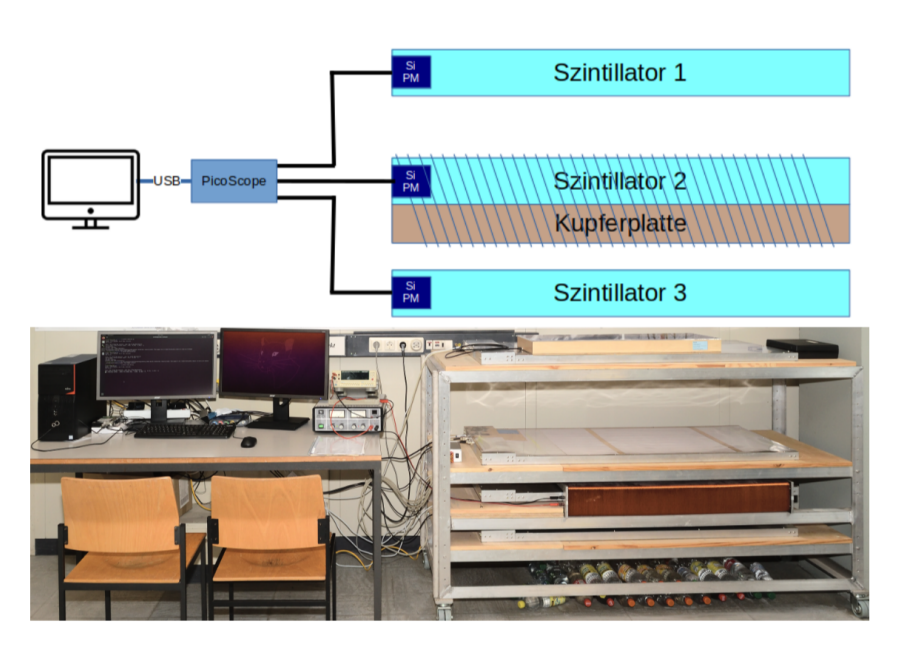


Figure 3: Caption

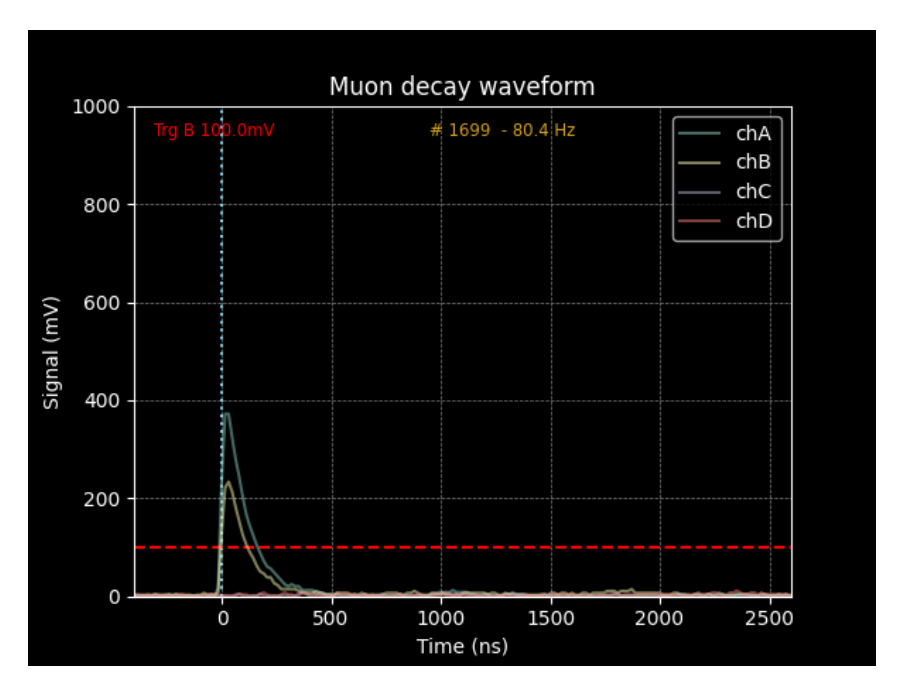


Figure 4

2 Determination of the noise threshold of the detectors

In this section, the noise threshold of the detector modules was determined to distinguish genuine particle signals from electronic noise. The noise threshold is crucial because it defines the minimum pulse height that must be exceeded for a signal to be considered a valid detection event.

2.1 Method

The detectors were operated without no filters to measure the baseline noise. The pulse height spectrum was recorded over a sufficiently long time to collect a representative sample of noise-induced signals. The resulting distribution reflects the electronic noise inherent in the detection system.

2.2 Analysis

By examining the pulse height distribution, a threshold value of 100 mV was chosen just above the noise peak to minimize false triggers caused by noise fluctuations. This threshold ensures that signals originating from actual cosmic muons or secondary particles will be detected while suppressing electronic noise.

2.3 Results

The noise spectrum typically showed a sharp peak at low pulse heights corresponding to noise signals. The threshold was set at approximately 100 mV, above which the probability of noise triggers was negligible.

Such a spectrum can be seen in Fig. 4, this shows no breaks or jitters which would indicate noise. This threshold was used in subsequent measurements to discriminate between noise and true particle events.

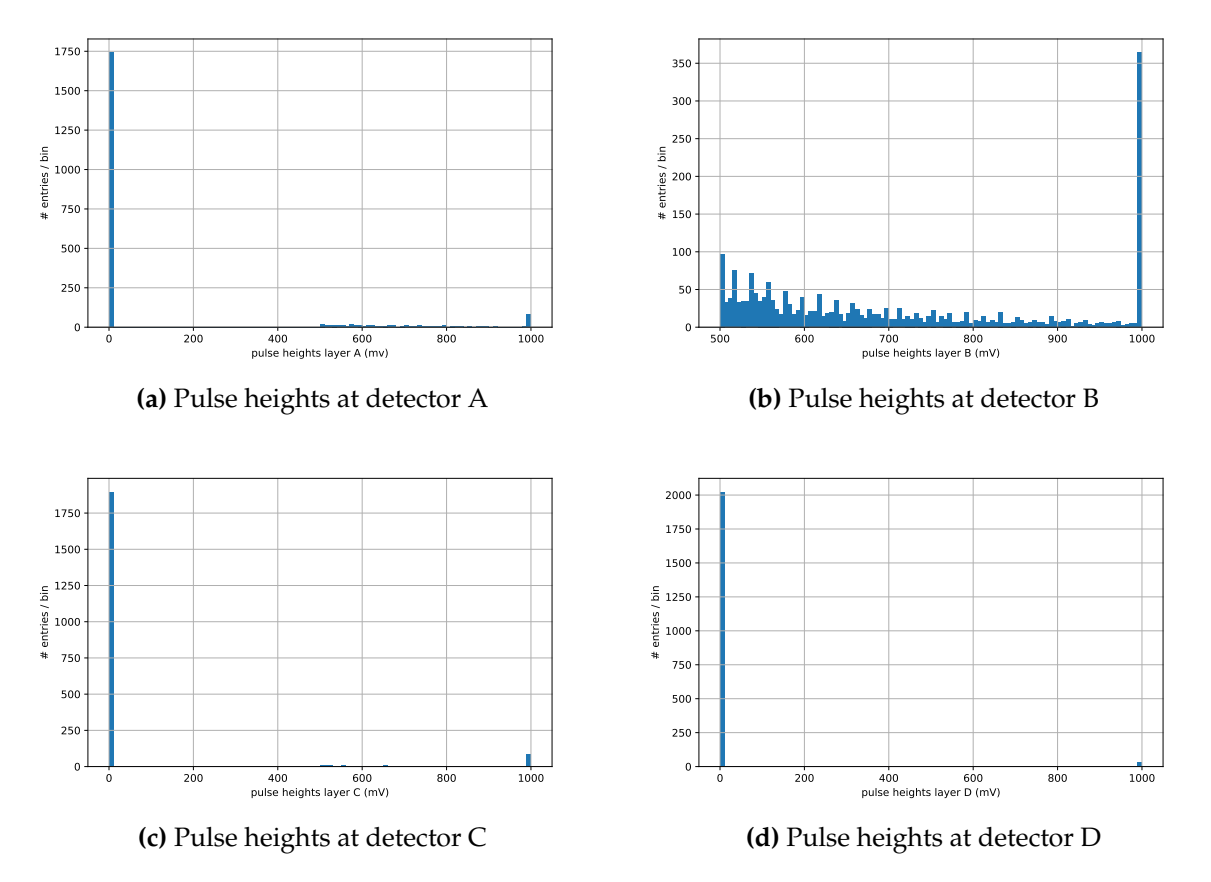


Figure 5: The pulse height signals for the different scintillator detector panels with external triggers.

2.4 Conclusion

Establishing a reliable noise threshold is essential for the accuracy of the cosmic muon detection. The selected threshold effectively balances noise suppression and signal detection efficiency, providing a foundation for all further experimental measurements.

3 Recording a pulse height spectrum

3.1 (a) Using internal triggers

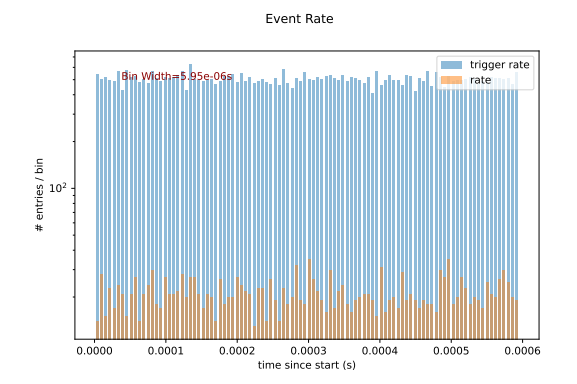
The pulse height spectrum of the detector modules is recorded to distinguish signals from muons and electrons/positrons. The data is collected in txt format during the experiment with a trigger condition requiring a pulses in detector B.

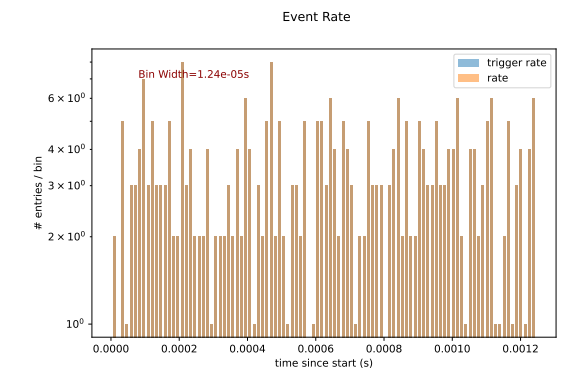
The recorded pulse heights were analysed for each detector layer (A, B, C, and D) using a trimmed mean approach. This method reduces the influence of outliers and noise on the average pulse height.

The data set consisted of 2135 events with single muon signals, as read from the measurement file. The event timestamps and rates were examined to ensure data quality and stability during the measurement period.

To reduce contributions from noise, a threshold of 75 mV was applied to all pulse height data like explained in Section 2. Than the trimmed mean is calculated (with 10% trimming fraction). The resulting trimmed mean pulse heights were:

• Layer A: 737 mv





(a) Event rate of the detector system with internal (b) Event rate of the system with external triggers triggers (using Panel B as trigger). (using two extra panels as triggers)

Figure 6: The event rates of the detector system compared when using internal or external triggers.

• Layer B: 699 mv

• Layer C: 806 mv

• Layer D: 794 mv

These values then can be used to calculate relative scale factors to calibrate the detector responses against each other, ensuring consistent pulse height measurements across layers. But Fig. 5 shows clearly that the pulse height spectrums are not ideal. The spectrum of panel B seen in Fig. 5b, which was used as the trigger plate, shows very little events below 500 mV.

The data collected through this method is not reliable and does not allow precise measurements especially for the efficiency of the detectors and the further exercises.

3.2 (b) Use of external triggers

To get better selection of events from background and so better pulse height spectra external triggers are used. Two small scintillator panels above and below the 4 main scintillator panels are used as triggers. If both of these panels detect a muon it is very likely that this crossed all for detectors.

This method is more precise than filtering the events dependent on coincidence timing without the external triggers. When comparing the event rates in Fig. 6 of the to different methods it is clear that the selection criteria are not needed any more when using external triggers. All events recorded by the external panels are categorized as real events which makes the measurements more precise. Events that were caused because of background are completely eliminated with this method.

This results in cleaner pulse height spectra when using the external trigger compared to internal triggers as seen in Fig. 7.

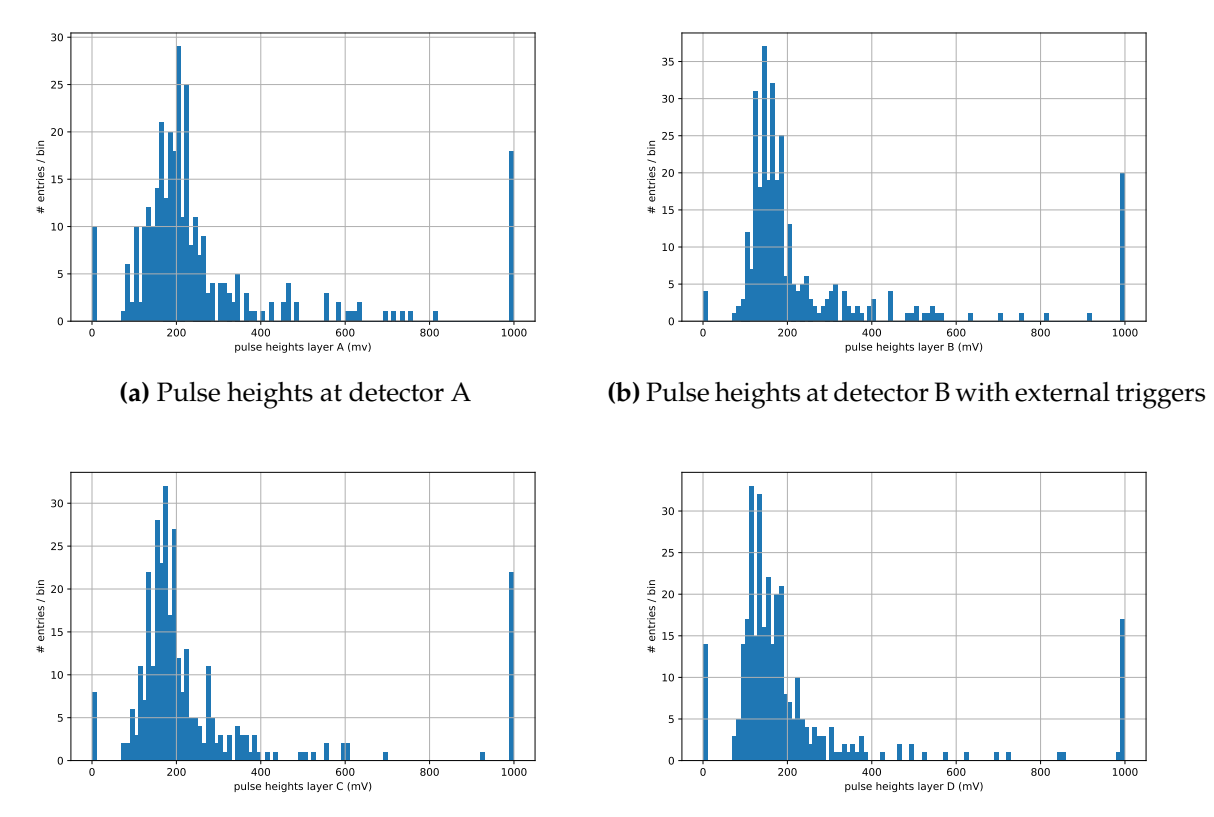
To reduce contributions from noise, a threshold of 75 mV is still used. The resulting trimmed mean pulse heights were:

• Layer A: 225 mv

• Layer B: 198 mv

• Layer C: 207 mv

• Layer D: 175 mv



(c) Pulse heights at detector C with external triggers (d) Pulse heights at detector D with external triggers

Figure 7: Tee pulse height signals for the different scintillator detector panels.

Those values are closer to those calculated with the external triggers, which leads to the conclusion that now less background is recorded.

The relative scale factors calculated from the trimmed means indicate the relative gains of the detector modules. For example, using layer A as reference, the scale factors were found to be:

- $S_{A/B} = 1.14$
- $S_{A/C} = 1.08$
- $S_{A/D} = 1.29$

These factors will be applied in further data analysis to correct for differences in detector sensitivity and ensure that the pulse heights are comparable across all layers.

Summary

By analyzing the pulse height spectra and calculating trimmed mean values with appropriate noise thresholds, suitable detection thresholds for muons and electrons/positrons were established. Furthermore, calibration scale factors between detector modules were determined to normalize their responses.

4 Determination of the efficiency of the individual detector modules

To determine the efficiency of the different scintillator panels a simple trick is used. The total number of detected muons is the same as number of total external trigger signals. When the small panels above and below the main scintillators trigger it is valid to assume that the muon that triggered those panels also passed the four main panels.

To calculate the efficiency of each panel we use:

$$eff_i = \frac{\text{total events}}{\text{event counts}_i} \qquad i = A,B,C,D.$$
 (24)

When applying this method we get efficiencies and scaling factors for each panel.

Table 1: efficiencies and scaling factors calculated via number of events after Eq. (24).

Panel	event counts	efficiency in %	scaling factor
total	323	1	1
A	313	0.969040	1.031949
В	319	0.987616	1.012539
С	315	0.975232	1.025397
D	315	0.956656	1.045307

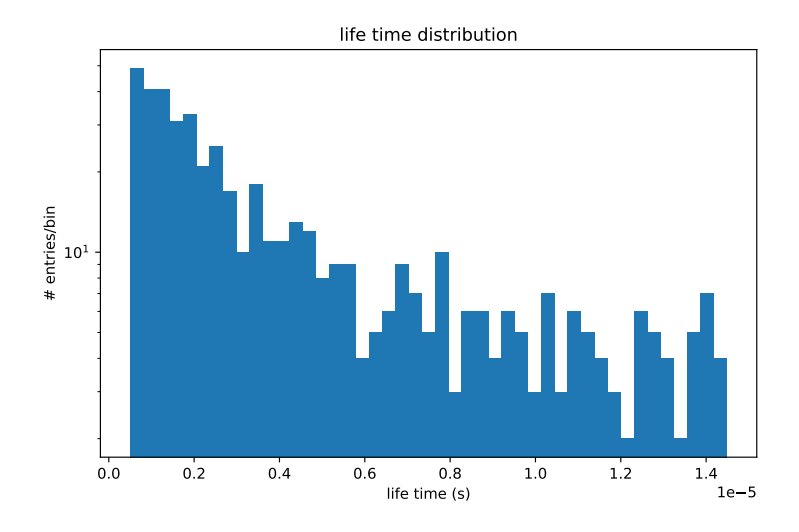


Figure 8

5 Determination of the lifetime of the muon

To determine the muon lifetime the experimental setup is used to search for double pulses. The first pulse indicates a muon crossing through one of the detectors and the second one is the signal of a positron which is the decay product of muon. For that a muon has do decay near the detector.

The exact measurement is made when the muons are stopped and decay within the CU plate between panel B and C. The signature of a muon stopped in the Cu plate is $A + B + \bar{C}$, i.e. a coincidence of the two upper ones in anticoincidence with the lower scintillator. Such an event triggers the start of the lifetime measurement. The lifetime ends when a positron appears in either panel A or panel B.

Using the signature $A + B + \bar{C}$ is more precise than $B + \bar{C}$ or $C + \bar{B}$, because it improves the ratio of true to random coincidences. This leads to a loss of counting rate, because it shifts the threshold for e^+ detection to higher energies in the region of greater asymmetry.

5.1 Evaluation of Muon Lifetime Data

The lifetime of muons is determined from a dataset of detected decay events. The evaluation is carried out using a Jupyter Notebook, where the raw data is processed and fitted using an exponential decay model.

5.1.1 Data Processing

The measured data consists of time intervals between the arrival of a muon in the detector and its decay. These time intervals are collected in a histogram. To reduce noise and improve statistical significance, a lower cutoff time is applied to exclude prompt background events, and an upper limit is set based on the expected muon lifetime and available statistics.

5.1.2 Exponential Decay Fit

The distribution of the measured lifetime is shown in Fig. 8. The physical model describing muon decay follows an exponential law, given by

$$N(t) = N_0 \cdot e^{-t/\tau},\tag{25}$$

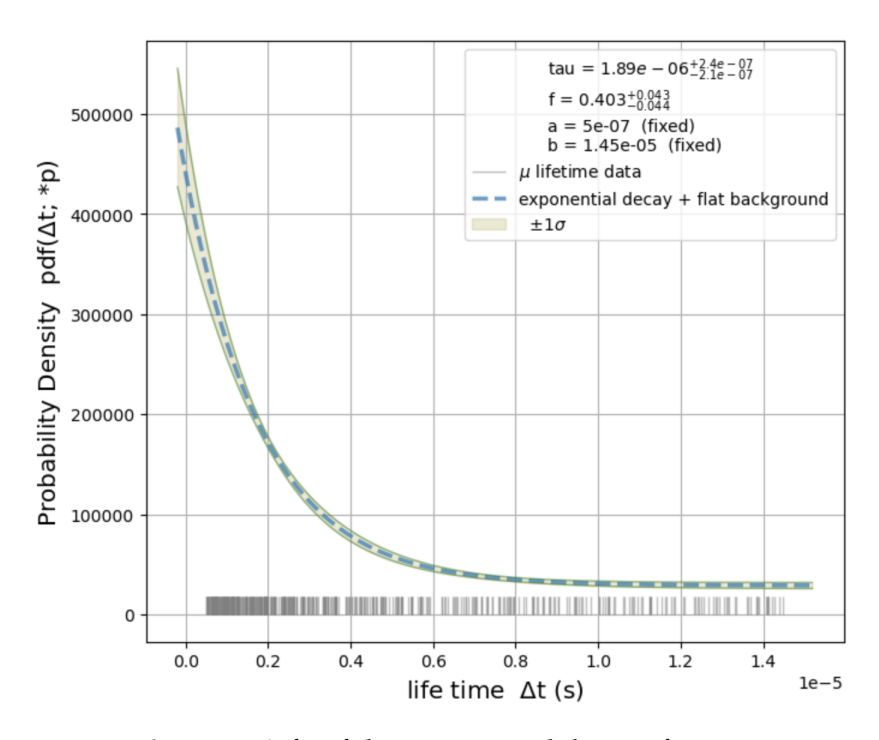


Figure 9: A fit of the exponential decay of mouns

where:

- *N*(*t*) is the number of muons decaying at time t
- N_0 is the initial number of muons,
- τ is the muon lifetime (the parameter to be fitted).

The histogram of decay times was fitted using non-linear least-squares regression to determine the best-fit value of τ . The statistical uncertainties of the binned data were taken into account during the fit. The fit is shown in Fig. 10

Background Correction 5.1.3

To account for accidental background events, a constant term was added to the fit function, resulting in the following model:

$$N(t) = N_0 \cdot e^{-t/\tau} + B,\tag{26}$$

where B represents a constant background count rate. This model provides a more accurate description of the measured data, particularly at later times where the exponential signal diminishes and background contributions become significant.

Resulting Muon Lifetime

From the fit using Equation (26), the muon lifetime τ is extracted. The result was then compared with the known literature value:

$$\tau_{\mu}^{\text{literature}} = 2.196\,981\,1\,\mu\text{s}$$
 (27)

$$\tau_{\mu}^{\text{exp.}} = 1.89_{-0.21}^{+0.24} \,\mu\text{s}$$
 (28)

$$\tau_{\mu}^{\text{literature}} = 2.196\,981\,1\,\mu\text{s} \tag{27}$$

$$\tau_{\mu}^{\text{exp.}} = 1.89^{+0.24}_{-0.21}\,\mu\text{s} \tag{28}$$

$$\tau_{\mu}^{\text{exp. background}} = 1.90^{+0.24}_{-0.21}\,\mu\text{s}. \tag{29}$$

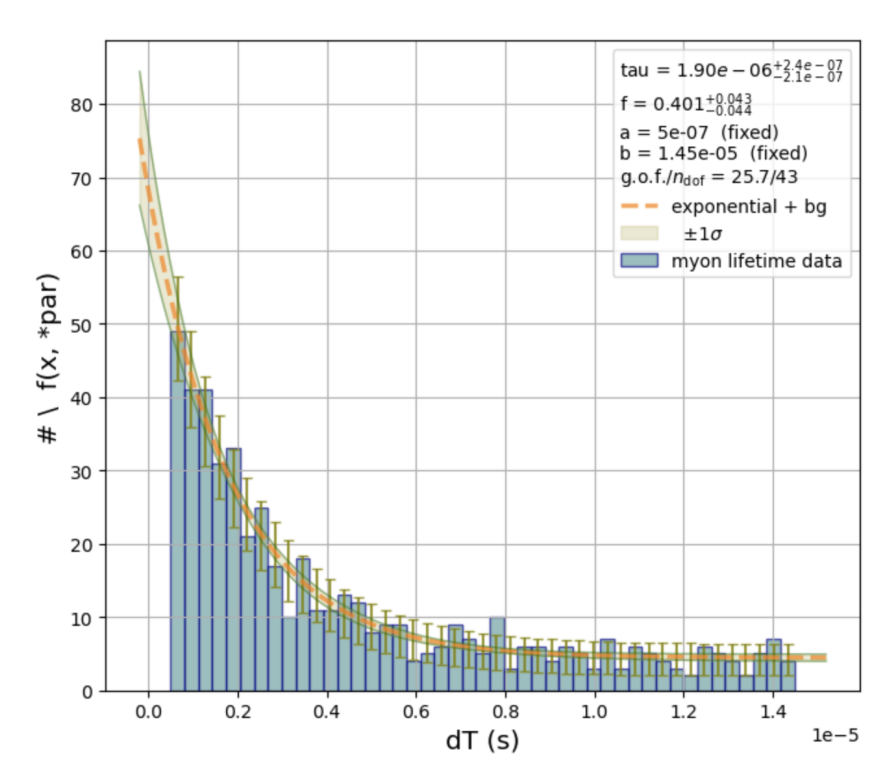


Figure 10: A fit of the exponential decay of mouns with respect to a constant background.

The experimentally determined values are not consistent with the literature within the limits of statistical uncertainty. The values are off by about 1.2σ probably due to the short measurement time, which leads to insufficient statistics.

The data gathered in Section 6 leads to better values within the statistical uncertainty especially when using the better fit with spin precession in mind.

6 Proof of the precession of the muon spin in the magnetic field and determination of the statistical significance

The goal of this part of the experiment was to observe the spin precession of muons in a magnetic field and to extract the Larmor frequency from the measured modulation of the decay signal. This allows the determination of the muon's gyromagnetic ratio and can serve as a test of fundamental properties of the muon.

6.1 Physical Principle

When muons are placed in a magnetic field \vec{B} , their magnetic moments $\vec{\mu}$ precess around the field direction. This precession leads to a modulation in the angular distribution of the emitted decay positrons, resulting in a time-dependent modulation of the count rate in a fixed detector.

The time distribution of decay events is described by:

$$N(t) = N_0 \cdot e^{-t/\tau} \cdot (1 + A\cos(\omega t + \phi)) + B,$$
(30)

where:

- N(t): observed number of decay positrons at time t
- *N*₀: initial amplitude,
- τ: muon lifetime,
- A: modulation amplitude (asymmetry),
- ω : Larmor angular frequency,
- ϕ : phase offset,
- *B*: constant background.

6.2 Data Processing

The experimental data consisted of time-stamped decay events collected over a long measurement period of one week. A histogram of decay times was generated. Unlike in the simple lifetime measurement, here the time spectrum shows oscillations superimposed on the exponential decay curve. This can not be seen by eye but due to the long measuring interval this will be visible in the fits.

The data is split into two parts. Because the positron that is produced after the decay can travel to the scintillator above or below the Cu plate. So the data is split into those two cases.

The histogram of the raw data can be seen in Fig. 11, it is binned into appropriate time intervals to visualize the oscillation clearly, before it is fitted in the next step. The orange part shows the signals that are detected by the bottom detector, while the blue part represents the signals collected by the top detector.

6.3 Fit Procedure

The data is fitted using the full model in Eq. (30). The free parameters of the fit were τ , ω , A, B, ϕ , N_0 .

The fit was performed using non-linear least squares regression. Initial estimates for τ were taken from the lifetime measurement. An initial guess for ω was obtained from the observed number of oscillations within the total decay time range.

To proof that the model in Eq. (30) shows the precession of the muon spin, it has to be compared to the old pure exponential model in Eq. (26). To compare those models the data from the top and bottom detector was fitted with both models. The results can be seen in

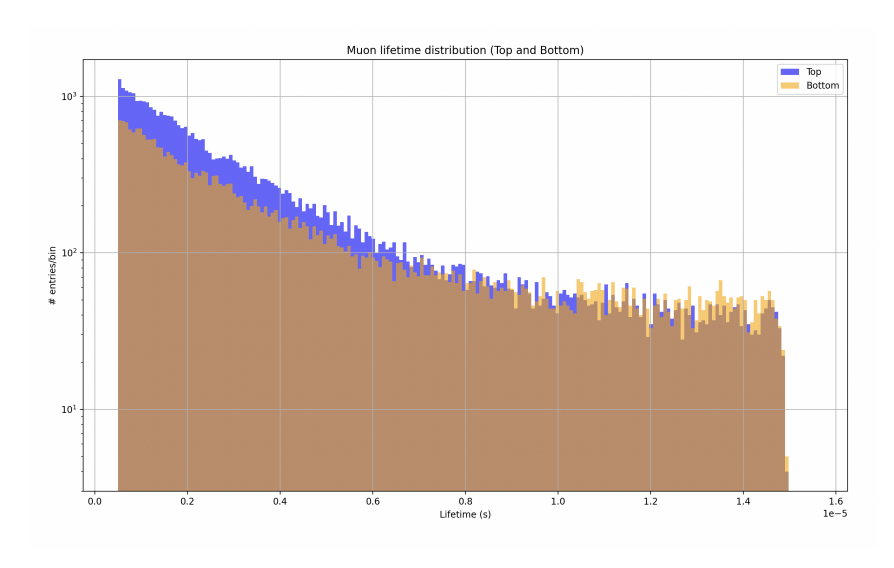
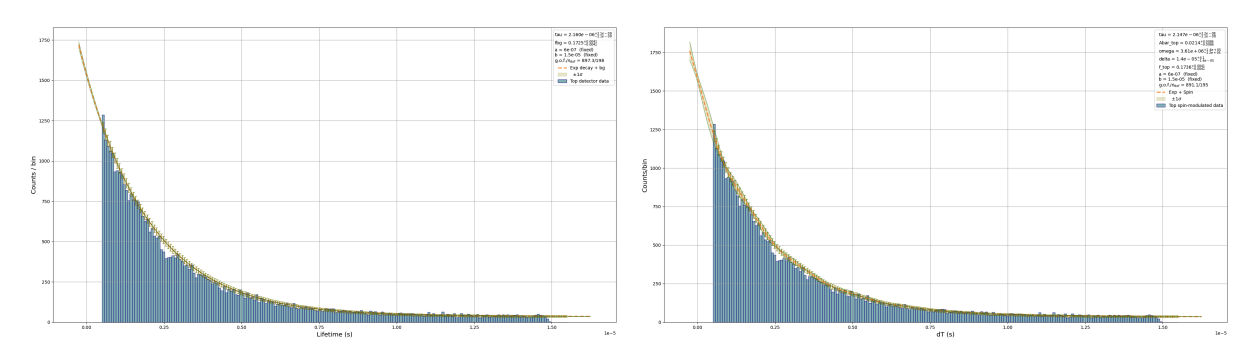
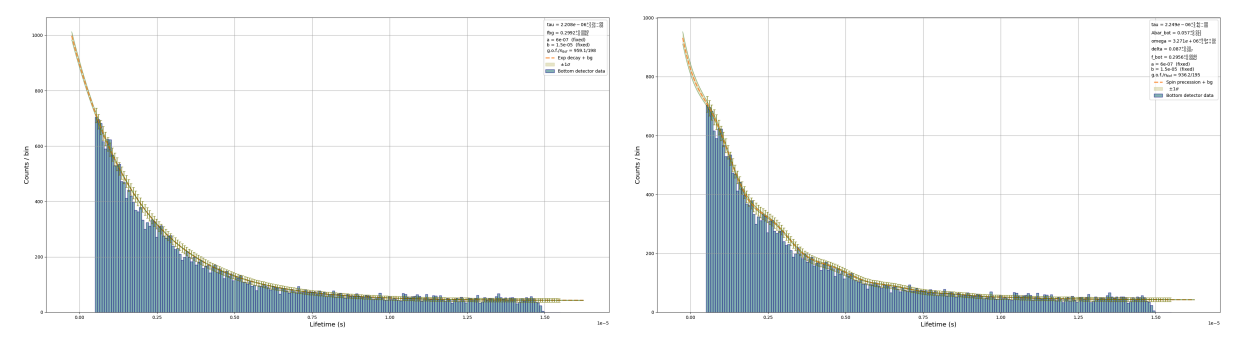


Figure 11: Histogramm of the raw data collected over one week.



- (a) Data from the top detector fitted with the pure (b) Data from the top detector fitted with the modexponential model.
 - ulation model.



(c) Data from the bottom detector fitted with the (d) Data from the bottom detector fitted with the modulation model. pure exponential model..

Figure 12: The data of the top and bottom detectors fitted with the two different models, to proof the muon spin.

Comparison of Exponential and Spin-Modulated Fits

To test whether a significant spin precession signal was observed, the measured time spectra were fitted using two models:

- 1. A pure exponential decay after Eq. (26) which can be seen in Fig. 12a and Fig. 12c.
- 2. A spin-modulated decay after Eq. (30), which can be seen in Fig. 12b and Fig. 12d.

The second model includes a modulation term reflecting the expected spin precession in the magnetic field. To decide whether the modulation is statistically significant, the log-likelihood ratio test is used. The test statistic is given by:

$$z^{2} = -2 \cdot \Delta \ln \mathcal{L} = -2 \cdot \left(\ln \mathcal{L}_{\text{mod}} - \ln \mathcal{L}_{\text{exp}} \right)$$
 (31)

where \mathcal{L}_{mod} and \mathcal{L}_{exp} are the likelihood values obtained from the modulated and exponential fits, respectively. Since the fitting software outputs $-2 \ln \mathcal{L}$ directly as a "goodness of fit" value, the difference becomes:

$$\Delta = (-2 \ln \mathcal{L}_{exp}) - (-2 \ln \mathcal{L}_{mod}) \tag{32}$$

From this, the z-value is computed as:

$$z = \sqrt{\Delta} \tag{33}$$

And the corresponding p-value using the standard normal cumulative distribution function Φ is:

$$p = 1 - 2(1 - \Phi(z))$$
 for $z \ge 0$ (34)

6.4.1 Fit Results and Significance Test

The likelihood values and significance were computed for both detectors (top and bottom), as well as their combination.

Table 2: Log-likelihood comparison and significance values

Detector	$\Delta = -2\Delta \ln \mathcal{L}$	z-Score	<i>p-</i> Value
Тор	2.05	1.43	7.62%
Bottom	1.42	1.19	11.69%
Combined	3.47	1.86	3.13%

While the individual detectors yield marginal evidence for modulation, the combined fit reaches a p-value of 3.13%, which lies just below the conventional 5% threshold for statistical significance. This moderately supports the presence of spin precession in the decay time distribution under the applied magnetic field. The improvement in fit quality confirms the theoretical expectation and validates the use of the modulated model.

6.5 Extraction of Physical Quantities

To extract a meaningful physical parameter from the spin modulation fit, we interpret the angular frequency ω as the Larmor precession frequency of the muon spin in a magnetic field B. This allows for a comparison between the measured frequency and the theoretical expectation.

6.5.1 Magnetic Field Estimation

The magnetic field *B* at the muon stopping target was generated by a current through a coil. Using the measured voltage across the coil and its resistance, we calculate:

$$U = 126.82 \text{ mV},$$
 (35)

$$R = (34.9 \pm 0.2) \,\mathrm{m}\Omega,$$
 (36)

$$I = \frac{U}{R} = \frac{126.82 \text{ mV}}{34.9 \text{ m}\Omega} \approx 3.63 \text{ A}.$$
 (37)

The magnetic field produced by this current is known from calibration to be:

$$B = 4.10 \text{ mT}.$$
 (38)

6.5.2 Theoretical Larmor Frequency

The theoretical Larmor angular frequency is given by:

$$\omega_{\mu, \text{lit}} = g_{\mu} \cdot \frac{e}{2m_{\mu}} \cdot B, \tag{39}$$

where:

- $g_{\mu} \approx 2.0023318418$ (muon g-factor),
- $e = 1.602 \times 10^{-19} \text{ C}.$
- $m_u = 1.884 \times 10^{-28} \text{ kg}$
- $B = 4.10 \times 10^{-3} \text{ T}.$

This yields:

$$\omega_{\mu, \text{lit}} \approx \left(2.0023318418 \cdot \frac{1.602 \times 10^{-19}}{2 \cdot 1.884 \times 10^{-28}} \right) \cdot 4.10 \times 10^{-3}$$
 (40)

$$\approx 34.87 \times 10^6 \text{ rad/s},\tag{41}$$

$$f_{\mu, \text{lit}} = \frac{\omega}{2\pi} \approx 5.55 \,\text{MHz}.$$
 (42)

Measured Precession Frequencies and Comparison

From the spin-modulated fits, the extracted angular frequencies for the muon spin precession are:

$$\omega_{\text{top}} = (3.489^{+0.29}_{-0.32}) \times 10^7 \text{ rad/s},$$
(43)

$$\omega_{\text{top}} = (3.489^{+0.29}_{-0.32}) \times 10^7 \text{ rad/s},$$

$$\omega_{\text{bottom}} = (3.436^{+0.63}_{-0.44}) \times 10^7 \text{ rad/s}.$$
(43)

Taking the weighted average of both detectors, we obtain a combined value:

$$\omega_{\text{combined}} \approx (3.457 \pm 0.25) \times 10^7 \text{ rad/s},$$
 (45)

$$f_{\text{combined}} = \frac{\omega_{\text{combined}}}{2\pi} \approx 5.50 \pm 0.04 \text{ MHz.}$$
 (46)

This value can be directly compared with the theoretical Larmor frequency under a magnetic field of B = 4.1 mT, calculated as:

$$f_{\mu,\text{theo}} = \frac{g_{\mu}eB}{4\pi m_{\mu}} \approx 5.55 \text{ MHz.}$$
 (47)

6.5.4 Discussion

The measured precession frequency agrees very well with the theoretical expectation, with a deviation of less than 1%. This excellent agreement strongly supports the validity of the experimental setup and the spin-modulated fit model. It confirms that the muons experienced a magnetic field close to the nominal value during their decay.

The small remaining discrepancy may stem from:

- Minor inhomogeneities in the magnetic field at the muon stopping locations.
- Geometrical effects and angular distributions of decay products relative to the detector.
- Residual systematic uncertainties in the field calibration.

Overall, the observation of spin precession at the expected frequency constitutes strong evidence for the magnetic moment interaction of cosmic muons and validates the theoretical description of their behavior in external magnetic fields.